This is a repository copy of *The microstructural evolution of CM247LC manufactured through laser powder bed fusion*.

White Rose Research Online URL for this paper:
https://eprints.whiterose.ac.uk/196611/

Version: Published Version

Article:

The Microstructural Evolution of CM247LC Manufactured Through Laser Powder Bed Fusion

J.F.S. MARKANDAY, K.A. CHRISTOFIDOU, J.R. MILLER, E.R. LIVERA, N.G. JONES, E.J. PICKERING, W. LI, Y. PARDHI, C.N. JONES, and H.J. STONE

Numerous challenges persist with the additive manufacturing of high γ' containing Ni-based superalloys such as CM247LC. Currently, significant cracking occurs during deposition of CM247LC components using laser powder bed fusion and during post-processing. Whilst post-deposition procedures seek to eliminate or minimise cracks, current procedures do not produce a microstructure suitable for service. This study systematically investigates the microstructural evolution of CM247LC manufactured using laser powder bed fusion following multiple post processing treatments. Phase and textural changes after each processing step were consistent with previous studies, although an additional Hf-rich and Cr-depleted segregation zone was identified along intercellular boundaries in the as-deposited condition, believed to be associated with the cracking propensity. Compositional modification of CM247LC including removal of Hf, reduction of C and addition of Nb eliminated the segregation zone but these changes were associated with an increased susceptibility to solidification and liquation cracking.

I. INTRODUCTION

OVER the last decade, there has been a significant uptake of additive manufacturing (AM) methods across a wide range of industrial sectors for the fabrication of metallic components.[1,2] These methods are highly versatile, allowing for greater design freedom and near-net-shape production, which can lead to improved component efficiency and reduced material wastage. Within the aerospace sector, the use of AM is particularly desirable as it can lead to components with reduced weight, as well as highly complex geometries that can be fabricated without the need for fasteners and joints or with intricate cooling channel architectures.[1,3] Among AM techniques, laser powder bed fusion (L-PBF) has received particular attention from the aerospace industry as it produces components with higher dimensional accuracies that require less post-process machining.[3–5]

Despite the advantages of additive techniques, there remain significant challenges with the deposition of high-performance materials, including Ni-based superalloys.[3,6] Specifically, the AM of Ni-based superalloys is often associated with stress-induced micro/macro cracking, pronounced texture and microstructural inhomogeneities.[3,4] To address these issues, significant research has been carried out with notable successes in overcoming the complications of residual stress and anisotropy through process control, post-processing regimes and the use of higher-quality precursors.[6–9] There has also been progress in eliminating cracking for superalloys that contain low volume fractions of the γ' and γ'' strengthening precipitates (20 to 40 pct) via L-PBF.[10–13] Whilst low strengthening precipitate fraction superalloys often have better processability, they offer inferior temperature capabilities when compared to alloys that contain higher γ' volume fractions (> 60 pct) such as CM247LC.[14,15]

Numerous cracking mechanisms, defined in the Supplementary information Figure S1, are associated with the deposition of high γ' superalloys including solidification, strain-age and liquation cracking, with strain-age and liquation cracking being the more difficult to control.[16–22] In certain circumstances, solidification cracking has been eliminated through the development of improved process control and the use of post-deposition techniques such as hot isostatic pressing

J.F.S. MARKANDAY, J.R. MILLER, N.G. JONES, and H.J. STONE are with the Department of Materials Science & Metallurgy, University of Cambridge, 27 Charles Babbage Road, Cambridge, CB3 0FS, UK. K.A. CHRISTOFIDOU, and E.R. LIVERA are with the Department of Materials Science and Engineering, University of Sheffield, Mappin St, Sheffield City Centre, Sheffield S1 3JD, UK. Contact e-mail: k.christofidou@sheffield.ac.uk E.J. PICKERING is with the Department of Materials, University of Manchester, Sackville Street Building, Manchester, M1 3BB, UK and also with the Henry Royce Institute, The University of Manchester, Manchester, M13 9PL, UK. W. LI, Y. PARDHI, and C.N. JONES are with the Rolls-Royce plc, PO Box 31, Derby, DE24 8BJ, UK.

(HIP).[19,23] More problematic are strain-age and/or ductility dip cracking, which are linked to the precipitation of the γ' phase in the presence of the high residual stresses generated during deposition due to the rapid cooling rates involved.[14,16,18] Research is still ongoing into determining a methodology to effectively overcome the occurrence of this type of cracking.[15,18,22,24,25] Liquation cracking is often attributed to a large freezing range, and the formation of low melting point films towards the end of solidification that may crack as a result of the developing solidification strain.[16–21] There have been reports that Hf-containing eutectics are a key contributor to liquation cracking in CM247LC and the elimination of this element has been shown to improve resistance to cracking in the AM of a number of Ni-based superalloys.[14,19,26] Even when crack-free parts are manufactured through careful control of the deposition conditions, the post-deposition operations of HIP and precipitation heat-treatments can still lead to extensive cracking, rendering the component unsuitable for service.[6,15] Therefore, it is critical to understand the microstructural evolution during post-processing operations, such that suitable parameters and post-processing regimes can be defined that avoid cracking and enable the use of L-PBF produced CM247LC components.[3,6] Consequently, this study characterises L-PBF produced CM247LC at each stage of the post-deposition sequence encompassing sand blasting, HIP, solution treatment and precipitation aging treatments to determine the microstructural changes that take place. Compositional modifications are also explored to gain further insights into the effect of Hf and C on the microstructural evolution of the material.

II. EXPERIMENTAL

Samples of CM247LC and CM247LC-Mod (Mod-1) were prepared by L-PBF using gas-atomized powder, the nominal compositions of which are given in Table I. For the Mod-1 composition, Hf was completely removed, whilst the concentration of C was significantly reduced from nominal CM247LC. A small amount of Nb was added to offset the loss of Hf, with the intent of retaining the nominal γ' content. For each composition, five thin plates were fabricated with dimensions given in Figure 1. The builds for each alloy were completed in the same deposition chamber under identical processing conditions using virgin powder. The deposition employed a linear scan strategy.

The five plates manufactured for each composition were investigated in different post-deposition conditions. The post-deposition steps used in this study are summarised in Table II, which comprise steps that are routinely applied to the preparation of CM247LC. The sand blasting process in step B was performed directly following deposition. Sand blasting was completed to close surface cracks and reduce surface roughness. This was performed at an industrial provider in accordance with current industrial practice. The HIP cycle utilised in step C was completed under Ar at a temperature of

1250 °C for 2 hours and a pressure of 140 MPa. For solution heat treatment, step D, samples were heated to 1250 °C and held for 2 hours, followed by gas cooling in the furnace. For the precipitate age, step E, the samples were heated to 870 °C, held for 16 hours and air-cooled. All samples were encapsulated in Ar-backfilled quartz ampoules prior to heat-treatment to minimise surface oxidation. For all heat-treatments, the samples were inserted into a pre-heated furnace and then air-cooled on the bench on completion of the prescribed heat-treatment, unless otherwise stated. The final treatment F was selected to cause full recrystallisation in the sample.

Electro-discharge-machining (EDM) was used to prepare specimens for microscopy. Specimens were mounted in conductive Bakelite and prepared to a 0.25 μm surface finish using standard metallographic techniques. A final chemical polish was performed for 5 minutes using a 1:5 solution of 0.04 μm colloidal silica in water. Light microscopy was completed on a CLEMEX microscope for the analysis of sample density. Thresholding of the images to quantify the total area fraction of cracks and pores was completed using ImageJ. In these analyses, the combined fraction of cracks and pores were considered when calculating the sample density.

An FEI Nova NanoSEM 450 scanning electron microscope (SEM) was used for characterisation of the microstructural and textural evolution. The microscope was equipped with an e⁻Flash1000 electron backscattered diffraction (EBSD) detector. EBSD orientation maps were acquired using a step size of 2 μm over an area of 3 mm^2. The Channel 5-HKL and MTex software packages were used for processing of the EBSD data. The kernel average misorientation (KAM) map was processed by first denoising the EBSD map with a half quadratic filter with a smoothing parameter of 0.5. Neighbours up to order 1 were considered in the KAM calculation with a threshold of 2.5 degrees. The pole figures were produced directly from the EBSD orientation data in the build direction with a heatmap colour range of 0 to 8 multiples of uniform density (mud). The sample dimensions labelled on EBSD figures correspond to the build direction (BD), scanning direction (SD) and transverse direction (TD), as defined in Figure 1. Further image processing and particle analysis was completed in the open-source ImageJ software.

A Bruker D8 X-ray diffractometer was used with a Cu-Kα source operating at 40 kV and 40 mA. Data were collected in the angular range of 30 to 80 deg (2θ) with a step size of 0.05 deg and a dwell time of 3 seconds. Samples were rotated at 30 RPM during the acquisition to improve counting statistics. The Topas academic software package was used for the analysis and fitting of the diffraction data.

A Netzsch 404 calorimeter was used to perform differential scanning calorimetry (DSC) on cylindrical specimens with a diameter of 5 mm and a thickness of 1 mm. Heating was performed at a rate of 10 °C/min to a maximum temperature of 1400 °C, followed by a 10-minute isothermal hold before cooling at the same rate. All data were acquired under flowing argon (~ 50 mL/min).

Higher resolution microstructural and phase analyses were completed using transmission electron microscopy (TEM). For the CM247LC samples an FEI™ Tecnai Talos TEM was used and for the Mod-1 specimen an FEI™ Tecnai Osiris TEM was used. For these studies, the TEM specimens were prepared using focussed-ion-beam (FIB) milling and were spot attached to a TEM grid. The TEMs were operated at 200 kV and were used to acquire electron micrographs and selected-area diffraction patterns (SADP). The TEMs were operated in scanning transmission electron microscopy (STEM) mode to perform energy dispersive X-ray spectroscopy (EDX) compositional analysis.

The elastic properties of the samples were measured using resonant ultrasound spectroscopy (RUS) following the methodology in the work of Migliori and Sarrao[27] and McKnight et al.[28] Parallelepiped specimens with dimensions $5 \times 4 \times 3$ mm were prepared via EDM. The faces of each specimen were hand polished to a finish of 4000 grit. RUS spectra, containing 50,000 data points, were collected at room temperature and frequencies between 100 and 1200 kHz. Four spectra were recorded for each specimen in different orientations to ensure that all resonances were observed. The Wavemetrics IGOR Pro software package was used to analyse the spectra and fit resonant peaks with an asymmetric Lorentzian function. For the determination of the elastic constants, the open-source rectangular parallelepiped resonances (RPR) code[27] was used for fitting of the recorded resonant frequencies. Orthotropic elastic symmetry was assumed for the samples and initial guesses for the elastic constants were derived from cast material. The experimental resonant frequencies were used to fit the elastic constants with a root-mean-square (RMS) error describing the quality of a fit. A reasonable fit was assumed for an RMS error of < 0.8 pct. Hill averages for the Young's and shear moduli were calculated from the elastic constants using the open-source EIAM code.[29] Graphs were derived from these data that describe the directional stiffnesses and anisotropies of the samples. An approach derived from the work of Ravindran et al.[30] was used to calculate anisotropy coefficients for the data. All data are given with respect to the specified directions of BD, SD and TD defined in Figure 1.

Table I. Nominal Compositions of the CM247LC and CM247LC-Mod Precursor Powder Used in this Study for L-PBF, Given in Wt Pct

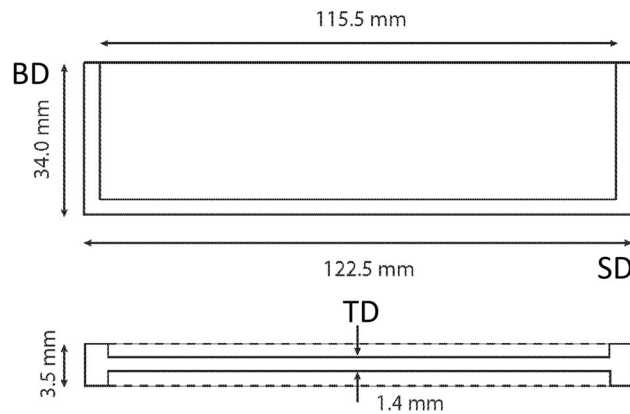|	CM247LC	CM247LC-Mod
Al	5.6	5.6
Co	9.2	9.2
Cr	8.1	8.1
Hf	1.4	0
Mo	0.5	0.5
Nb	0	0.7
Ni	bal.	bal.
Ta	3.2	3.2
Ti	0.7	0.7
W	9.5	9.5
C	0.07	0.01
B	0.015	0.015
Zr	0.015	0.015

Fig. 1—Schematic diagram of L-PBF thin plate samples. The samples were fabricated with the height (34.0 mm) corresponding to the build direction (BD) and the widths (3.5/1.4 mm) corresponding to the laser scanning direction (SD). The lengths (122.5/115.5 mm) correspond to the transverse direction (TD).

III. RESULTS

A. *Microstructural and Crack Analysis*

Back-scattered electron (BSE) images of L-PBF CM247LC following each stage of standard post-processing (steps A to E) are given in Figure 2. Images were

Table II. Details of the Post-deposition Steps Applied to Each Sample

Condition	Details
A	As-deposited
B	A + sand blasted
C	B + HIP at 1250 °C/2 h and 140 MPa
D	C + solution heat-treatment at 1250 °C/2 h
E	D + precipitate age at 870 °C/16 h
F	C with solution heat-treatment at 1260 °C/2 h and precipitate age at 870 °C/16 h

taken from the central region of the build, representative of the bulk microstructure. No significant variations in microstructural features were observed with build height. Additional light microscopy images at a low magnification and SEM micrographs of the samples have been provided in the Supplementary information.

In the as-deposited state, a typical cellular structure was observed. Although, not apparent from Figure 2 a significant level of cracking was observed, consistent with previous reports.[31] SEM images of selected cracks present in the microstructure following each processing step are provided in the Supplementary information, see Figure S1. Additionally, a crack morphology table has been provided in the Supplementary information to assist with crack identification, see Table S1. No distinct microstructural differences could be identified between the bulk material following steps A and B. This is reasonable, as sand blasting only affects the surfaces to a depth of approximately 200 μm. Significant cracking was observed in material in both the A and B conditions, with multiple morphologies identified. The average density of the bulk microstructure for A and B condition was measured to be 99.7 ± 0.05 pct. Sand blasting removed the majority of surface cracks on the samples, though there was no change in crack area fraction for the bulk microstructure. The observed morphology of the cracks was consistent with solidification and liquation cracking and is typical for additively manufactured CM247LC.[14,16,17,22,32] Additional SEM images of the sand blasted region have been provided in the Supplementary information, see Supplementary Figure S3. This analysis indicated that sand blasting had reduced the fraction of surface cracks present in the A condition. However, material deeper below the surface was unaffected by this process and so the bulk sample density in condition B remained the same as condition A.

For all specimens, phases could be observed to have formed along the (sub)-grain boundaries, Figure 2. Segregation of elements to these regions is commonly observed in as-deposited L-PBF Ni-based superalloys.[19] Additionally, carbides have been reported to be present in these regions in the as-deposited condition for CM247LC. Further analysis of these regions and particles in the as-deposited condition (A) has been presented in a later section.

Following the HIP treatment (C), there has been partial recrystallisation but with the microstructure remaining largely cellular. Additionally, the phases
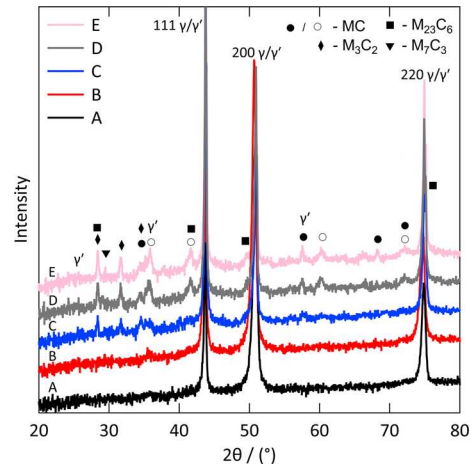

Fig. 3—XRD patterns of L-PBF CM247LC in the post-processing conditions specified in Table II. The patterns have been offset vertically for clarity and the intensity axis is scaled by √I to enable low intensity peaks to be identified. The positions of the diffraction peaks from the primary phases present have been labelled. Two distinct types of MC carbide were identified, with the filled circles corresponding to the (Ta,Ti)C reflections and the unfilled circles correspond to the (Hf,Ta)C.
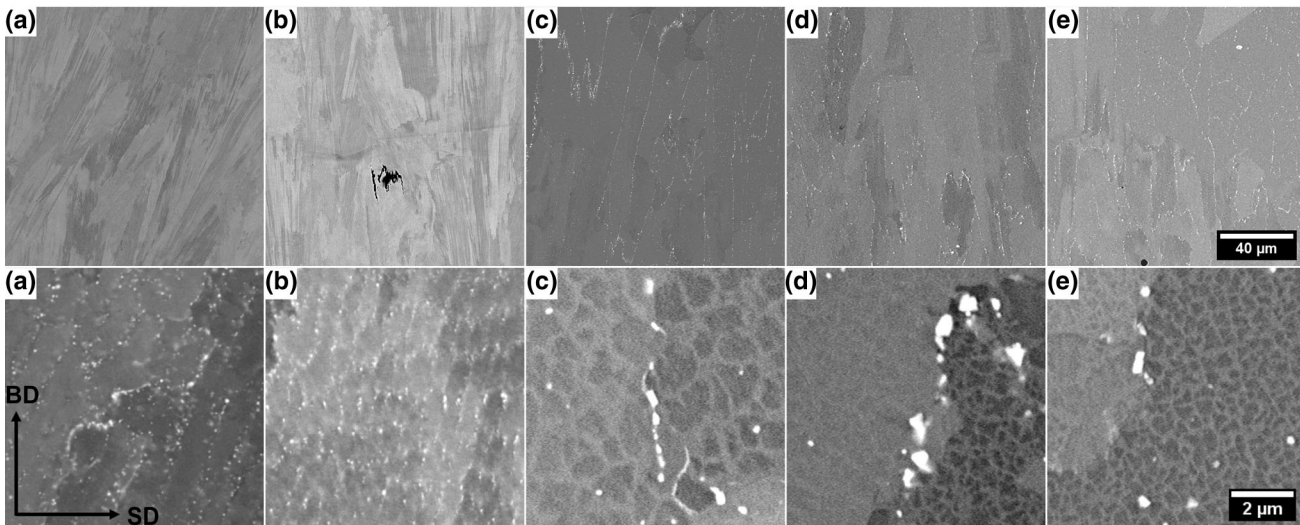

Fig. 2—SEM analysis of L-PBF CM247LC at each step of standard post-processing (steps *a* to *e* in Table II). Two BSE images have been provided; (top row) a low magnification image of the general microstructure and (bottom row) a high magnification image of areas near a grain boundary. The build direction (BD) and scanning direction (SD) have been identified in the bottom left-corner.
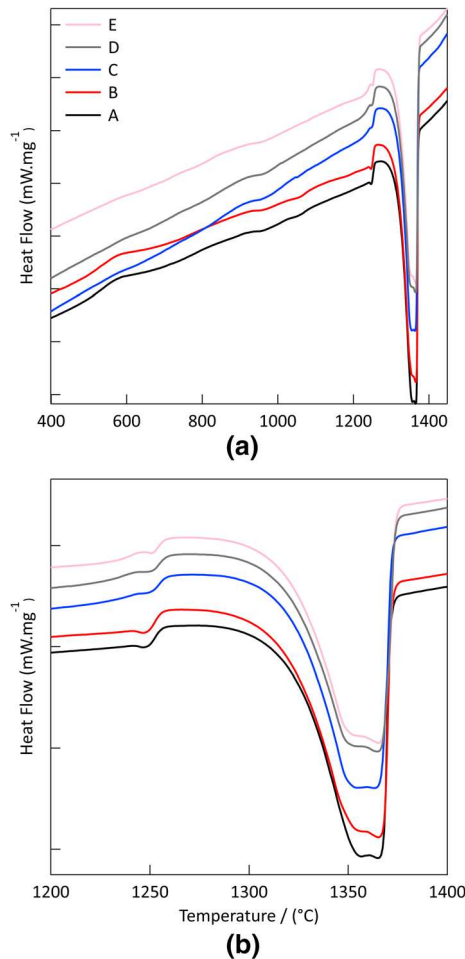
Fig. 4—(a) DSC traces for the first heating of L-PBF CM247LC specimens in conditions A to E from room temperature to 1400 °C. Each trace has been vertically offset for clarity. (b) A magnified section of the terminal region of the traces to highlight the differences between the samples on melting.

decorating the cellular boundaries observed in the A and B conditions reduced in number density and coarsened significantly, as well as no longer correlating with all of the original cellular boundaries. Irregularly shaped γ' precipitates were also visible in the high magnification images acquired. Notably, the HIP cycle (C) reduced the apparent prevalence of cracking, with the sample density being 99.94 ± 0.05 pct. However, some solid-state cracks were identified within the sample following the HIP cycle. The presence of such cracks following heat-treatment has been reported extensively in the literature.[14–16,19,33]

Following solution heat treatment (condition D), there was evidence of additional recrystallisation. It was observed that the spherical sub-grain bright phase had coarsened further. The average sample density (99.96 ± 0.05 pct) remained similar to that observed in condition C. In the higher magnification image, coarsened γ' precipitates are visible.

After aging (condition E) coarsening of the γ' precipitates had occurred. The bright phase was also observed to remain present, with little further coarsening

apparent. As with condition D, the average sample density (99.96 ± 0.05 pct) remained comparable to that observed in condition C.

B. Phase Analysis

Crystallographic identification of the phases present in each condition (A to E) was performed using the XRD patterns presented in Figure 3. The positions of reflections from the primary phases present have been identified with markers. In the A and B conditions, only reflections from the γ matrix, which overlap the fundamental reflections from the γ', could be identified. Following the HIP treatment (condition C), reflections consistent with $M_{23}C_6$ and M_3C_2 carbide phases appeared in the patterns. After the solution heat treatment (condition D) reflections from two additional MC type carbide phases were present in the diffraction pattern, which from literature may be the (Ta,Ti)C and (Hf,Ti)C carbides.[34,35] In condition E, an additional reflection believed to arise from the M_7C_3 carbide phase was also observed in the diffraction data.

The presence of borides was not indicated from the XRD analysis as attempts to fit the patterns using structural information from common borides were unsuccessful. From condition A to E there are noticeable changes in the widths of the peaks from the γ matrix, suggesting a relaxation of residual stresses or increase in compositional homogeneity. In addition, the intensities of the γ reflections are suggestive of an intense residual texture. For conditions C, D and E a lattice misfit of ≈ 0.28 pct was calculated from the lattice parameters of the γ and γ' phases, determined through Pawley analysis.

Further analysis of the samples was conducted using DSC, with the traces obtained on heating for all conditions of the L-PBF CM247LC presented in Figure 4. For all samples, similar transition events were observed. In the data acquired from conditions A and B an endothermic event begins near 550 °C, which is believed to be associated with the formation of the γ' precipitates. This peak is commonly observed in the first heating of additively manufactured Ni-based superalloys in the as-deposited condition.[12,15] An endothermic event starting near 1250 °C for samples A to C is observed and is likely to be associated with the dissolution of the γ' precipitates. For all samples, the solidus and liquidus points are approximately 1280 °C and 1380 °C, respectively, giving a freezing range of 100 °C. An endothermic event at 1350 °C is observed for all samples and may be attributed to the dissolution of the MC-type carbides.[15,34] The presence of the MC carbide phase is expected in all conditions. However, the reflections were not resolved in the XRD for specimen A to C due to the low volume fraction. Confirmation of the presence of this phase was completed using TEM.

The microstructure and phases present in the as-deposited (A) and fully aged (E) samples were investigated further using TEM and STEM-EDX. The results of the TEM analysis for L-PBF specimens in conditions A and E are given in Figures 5 and 6 respectively. A high-angle grain boundary was selected as a location for the TEM
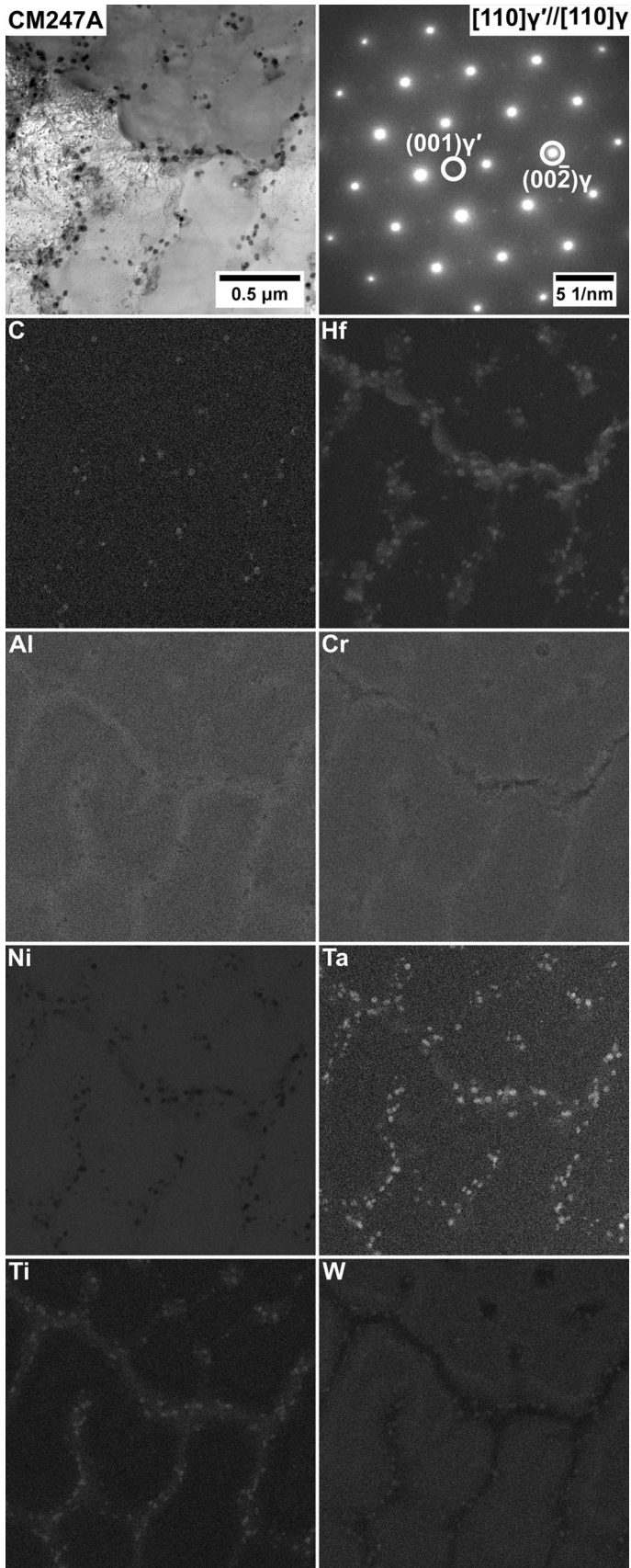
CM247A

[110]γ′//[110]γ

(001)γ′ (002̄)γ

0.5 µm

5 1/nm

C

Hf

Al

Cr

Ni

Ta

Ti

W

analysis on the samples. The distribution of C and Hf along the grain and intercellular boundaries was of interest due to the link with cracking behaviour identified in the literature.[19,26,36,37] For both samples, the selected-area diffraction pattern (SADP) taken from the matrix indicates the presence of the γ' phase, albeit it was not possible to resolve the γ' phase in the STEM images for condition A. In the as-deposited sample, the STEM-EDX maps indicate a general enrichment of Al, Hf, Ti and to a lesser extent Ta to the intercellular regions. In addition, there are discrete locations near or in the intercellular regions that are rich in C, Hf, Ta and Ti. The enrichment in the γ'-forming elements; Hf, Al, Ti and Ta, and the strong depletion of Cr along the high-angle grain boundary would suggest that a continuous segregation region with a γ'-type composition has formed along the grain boundary. Discretely formed, spherical carbides rich in Hf, Ta, Ti and W can be identified along the grain and cellular boundaries. Their composition and morphologies are consistent with MC-type carbides, and SADPs confirm these to be crystallographically consistent with MC carbides as well.[34,38] There is also noticeable segregation of W to the intercellular regions and local enrichment at carbide locations.

TEM analysis of the fully aged sample, Figure 6, shows the presence of cuboidal and irregular-shaped γ' precipitates. Fan-type precipitates can be seen to have formed in the right-most grain. The elemental segregation to and around the γ' precipitates was consistent with previous work on aged CM247LC.[35] There was also segregation of Hf, Ta, Ti and W to spherical MC-type carbides that have formed discretely in the microstructure. The carbides are larger than those observed in the as-deposited condition and there was a shift in the morphology to cuboidal particles. A phase rich in Cr and W was also observed to have formed along the grain boundary. This phase has previously been identified as an $M_{23}C_6$ phase in the literature. However, it is possible that this is a mixture of different carbides that include the $M_{23}C_6$ and MC phases as reported in the literature.[35,39–41] Although not as clear as the partitioning to the MC carbides, the C EDX map also showed an enrichment in this location relative to the matrix.

Confirmation of the crystallography of these phases was achieved through selected-area diffraction, Figure 7. Two patterns have been provided for the MC-type carbides along the [100] and [112] zones, with the [112] provided for distinction against the [112] of the matrix phase. An orientation relationship of $[100]_{MC}\|[110]_\gamma$ was found between the MC-type carbides and the gamma matrix, whilst a $[113]_{M_{23}C_6}\|[112]_\gamma$

orientation relationship was identified between the $M_{23}C_6$-type carbide and the matrix. An additional carbide phase, M_7C_3, was identified from the diffraction analysis with the [011] pattern presented in Figure 7. The pattern for this phase was identified directly next to that of the $M_{23}C_6$ phase. No orientation relationship was found between this carbide and the matrix. The results are consistent with the XRD data in Figure 3 from CM247LC in condition E. The M_7C_3 carbide phase is not commonly reported for CM247LC. Its occurrence is therefore putatively attributed to the transformation of the carbide species from the initial MC carbide towards the $M_{23}C_6$ carbide *via* the M_7C_3. This is supported by the observation of the M_7C_3 only in proximity to the $M_{23}C_6$. However, unambiguous determination of the structures and compositions of the equilibrium phases would require further studies of samples subjected to prolonged exposures at high temperatures.

C. *Textural and Elastic Anisotropy Analysis*

The evolution of the microstructural texture of CM247LC following the post-processing steps was investigated using SEM-EBSD. The EBSD data acquired for the samples in all microstructural conditions specified in Table II have been presented in Figure 8. Samples were taken from the centre of each build, with an edge region visible. For each condition an inverse pole figure (IPF) map taken with respect to the build direction is provided with a corresponding set of pole figures. Using these data the texture of the samples can be described. In addition, the KAM map showing the degree of local misorientation has also been provided for each specimen. In condition A, a strong texture along the build direction is observed. The primary textural component is [001], with a lesser [011] component. These results are consistent with additively manufactured Ni-based superalloys.[12,42] There is also a high degree (3 to 5 deg) of misorientation within the columnar grains in the as-deposited condition. The results for condition B are similar to condition A, which is reasonable as sand blasting is not expected to promote microstructural changes within the bulk of Ni-based superalloys. However, the deformation induced by sand blasting did locally influence the recrystallisation behaviour near the sample edge,[43,44] shown at the top of each image. The results for condition C demonstrate that the HIP cycle has not induced additional recrystallisation within the bulk of the sample. In this condition, the texture component of the columnar grains has remained predominantly [001], with alignment along the build direction. The degree of misorientation within the grains has also remained comparable following the HIP treatment.

Following the solution heat treatment, condition D, the extent of the recrystallised region near the edge of the sample has increased. The recrystallised grains in this region have a low misorientation and no predominant texture. Partial recrystallisation is also observed within the bulk of the sample. As with condition C, the bulk texture has remained with a pronounced [001]
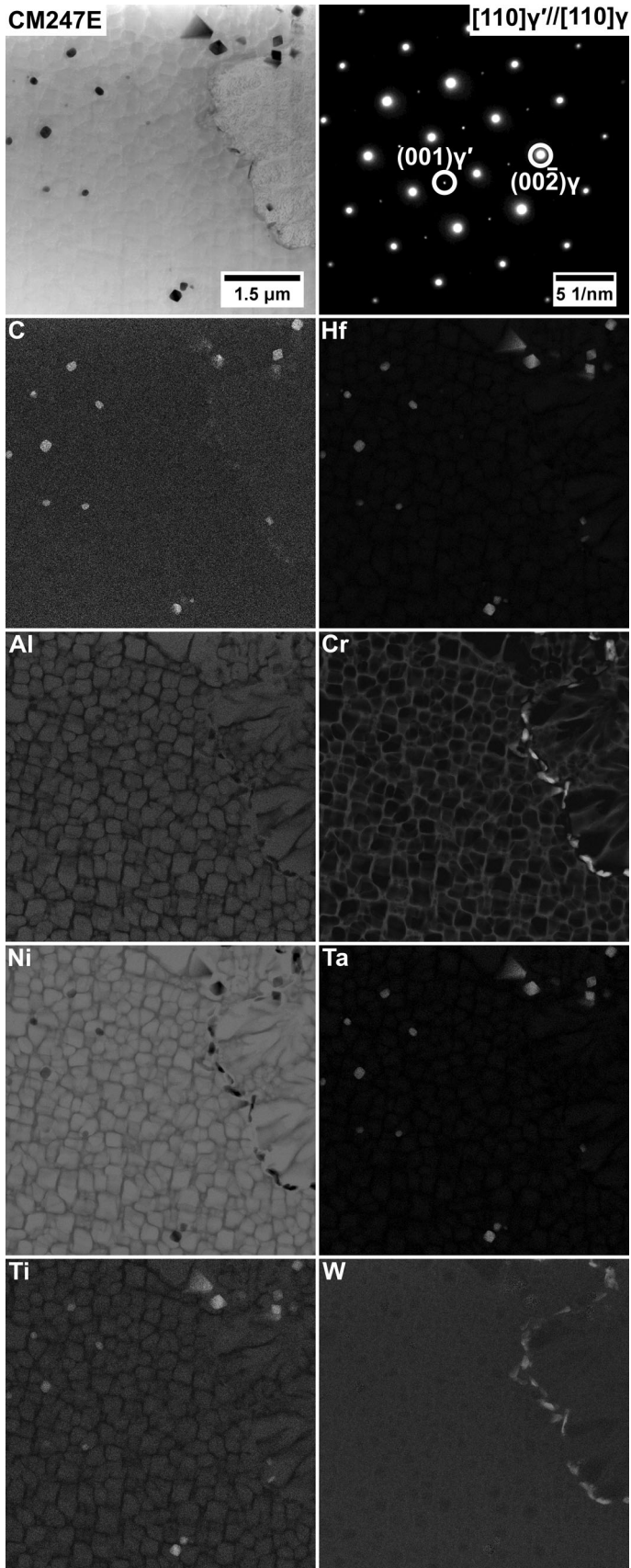
◄Fig. 6—TEM analysis of L-PBF CM247LC in the heat treatment E condition. A bright field electron image is shown at the top left; accompanied by a selected-area electron diffraction pattern for the matrix along [110] at the top right. Below are elemental distribution maps determined by STEM-EDX.
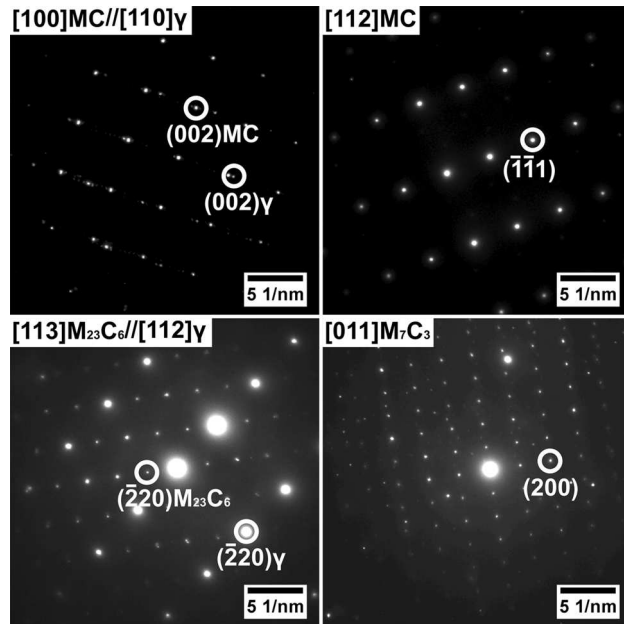

Fig. 7—Selected-area diffraction patterns (SADPs) for L-PBF CM247LC in condition E. For each pattern, the corresponding phase(s) and zone axes have been identified. Individual reflections have been marked on each pattern and orientational relationships provided where possible.

component down the build direction, though the [011] component was observed to decrease. The intragranular misorientation within the columnar grains has also remained constant. The results for condition E are consistent with that of condition D. This is to be expected as the relatively low temperature of the ageing would not be expected to promote grain growth or recrystallisation. Similarly, the level of misorientation within the columnar grains has remained high.

The microstructures observed in the specimens in conditions B to E are not homogeneous, with partial recrystallisation observed. The post-processing protocol was therefore altered to induce more complete recrystallisation using a higher solutioning temperature of 1260 °C, condition F. The SEM-EBSD analysis of material in this condition, shown in Figure 8, indicates that recrystallisation has occurred accompanied by significant grain growth. There are localised hotspots in the pole figure, possibly indicative of a [111] recrystallisation texture component along the build direction However, it is significantly weaker than the textures seen in the non-recrystallised conditions and likely a result of the large grain size observed in the sample. Additionally, the local misorientation within the grains has been reduced to < 1 deg. Notably, the sand-blasted region has remained, with a refined recrystallised grain

structure being observed near the edge of the sample (shown at the top of the image). There is a marked absence of twins within the bulk recrystallised microstructure.
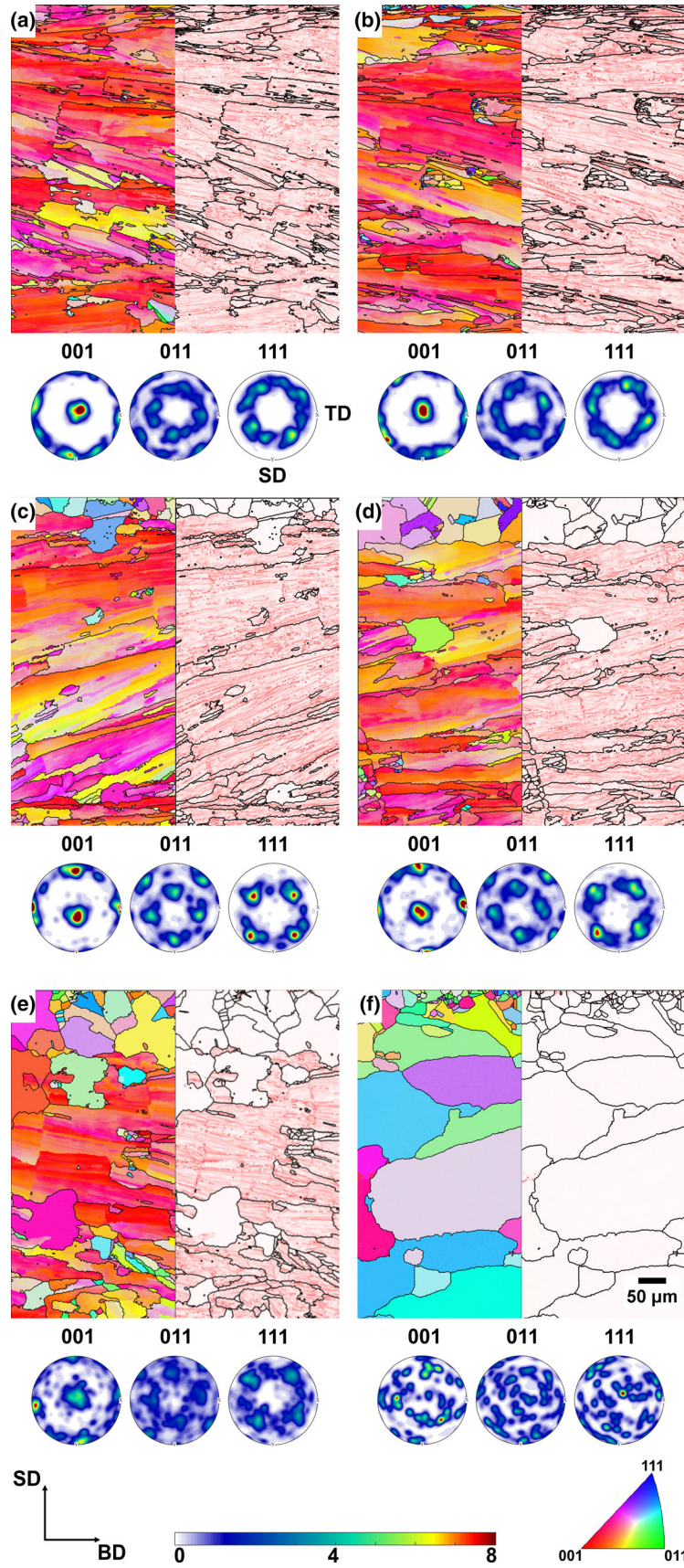
To further probe the evolution of the texture of the specimen with post-processing, RUS was used to measure the elastic properties. The orientation dependence of the Young's modulus for specimens A, E, and F are given in Figure 9. The elastic constants used to generate this plot are given in Table III. These data indicate that the specimen in condition A has strong orientational dependence of the elastic modulus. The elastic constants have symmetry that is close to being axisymmetric. In part this may be expected given the significant level of texture aligned along the build direction, although similarity between the TD and SD elastic constants was not necessarily expected.[12,34]

The orientational dependence of the modulus for the specimen in condition E shown in Figure 9 continues to exhibit appreciable anisotropy, with a small shift towards axisymmetric symmetry. In this condition, the Poisson's ratio and moduli are similar to that of the specimen in condition A, reflecting a minimal change in the elastic properties. In contrast, the trace in Figure 9 for the specimen in condition F shows a significant reduction in the directional dependence of the elastic modulus, though the axisymmetric symmetry remains prominent.

D. Modification of CM247LC

The results presented thus far highlight the challenges associated with the additive manufacturing of CM247LC. Two prominent issues are cracking during build and achieving microstructural control whilst seeking to mitigate cracking through post-processing. It has been well reported that the concentration of minor elements strongly influences hot cracking in Ni-based superalloys[14,16,45] and there has been significant research to understand this relationship in additive manufacturing and welding.[16,24,25] Of the elements that have been implicated in cracking propensity, Griffiths et al.[19,26] showed that Hf may contribute to cracking during additive manufacturing. The authors were able to show that a significant reduction in crack density could be achieved by near removal of Hf and process control. Indeed, recent research within the aerospace sector has indicated that removal of Hf from CM247LC might increase additive manufacturing processability.[46] However, complete removal of the Hf reduces the volume fraction of the γ′ precipitates, which will affect the mechanical performance.

In addition, it has been well established that propensity to hot cracking is significantly dependent upon the solidification behaviour.[16,24,25] Several authors have demonstrated that solidification cracking can be mitigated through manipulation of the final stages of solidification in line with theories developed for conventional casting.[14,21,26,47] Recently, Tang et al.[14] utilised a solidification cracking index developed by Kou et al.[22] that described the susceptibility to cracking based on solidification behaviour. In general, alloys

001 011 111

TD

SD

001 011 111

001 011 111

001 011 111

001 011 111

001 011 111

50 μm

SD

BD

0 4 8

111

001 011

Fig. 8—SEM-EBSD analysis of L-PBF CM247LC specimens in post-processing conditions (*a* to *f*). These conditions are detailed in Table II. Samples were taken from the centre of each build, with an edge region visible. For each sample an IPF map oriented along the build direction has been stitched with the corresponding KAM map. In addition, cubic pole figures oriented down the build direction have been provided for each sample below the maps.
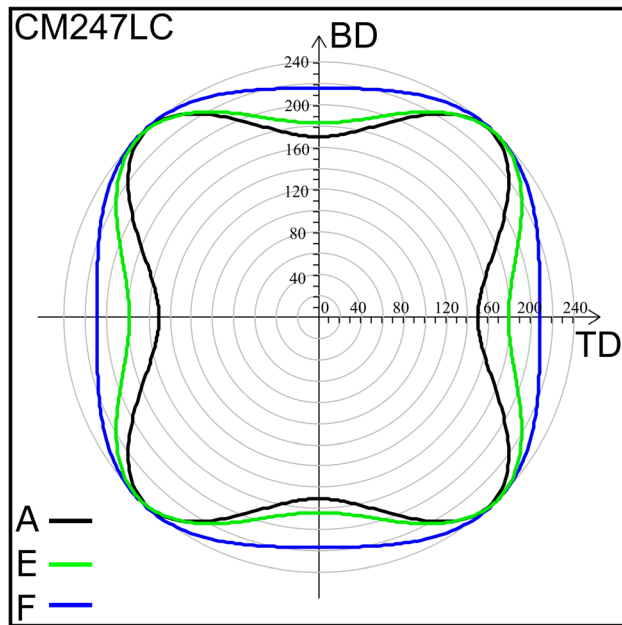

Fig. 9—The orientation dependence of the Young's modulus for L-PBF CM247LC specimens A, E and F with respect to the TD and BD.

containing terminal eutectics and smaller freezing ranges tend to display a resistance to solidification cracking.[16]

In this study, the effect of Hf on CM247LC was investigated through the removal of Hf in Mod-1. Nb addition was used to retain the mechanical properties through maintaining the γ' content, and reduced C content was utilised to understand the effect of carbide phases on recrystallisation behaviour. These compositional modifications were guided by equilibrium phase fraction predictions for the γ' and MC carbide phases using the ThermoCalc™ software.[48] Complete removal of Hf in the modified composition was predicted to reduce the γ' content. As such, 0.7 wt pct of Nb was added to maintain an appropriate γ' phase fraction of > 60 pct at 800 °C. The predictions indicated that a reduction in the C content of 0.6 wt pct would reduce the occurrence of MC and additional carbides by 90 pct. The reduced occurrence of MC and additional carbides was expected to modify the recrystallisation behaviour of the material by reducing the Zener drag. A lower recrystallisation temperature would likely result in less grain growth during post-processing. This composition was designated Mod-1.

XRD data from a sample of Mod-1 following processing to condition E (Table II) are given in Figure 10 along with data acquired from CM247LC in

the same state for comparison. These data support the hypothesis that the carbide volume fraction has been reduced, with no distinguishable reflections from carbide phases for the Mod-1 composition. The only prominent reflections in the Mod-1 diffraction pattern are from the γ and γ' phases, although the precipitate superlattice reflections have not been resolved.

Further analysis was completed using DSC, with the results for the as-deposited material presented in Figure 11. The DSC thermogram indicates that the Mod-1 has a decreased freezing range by 14 ± 2 °C. In the magnified section (B) a small endothermic event can be identified occurring at 1355 °C. This is similar to the CM247LC MC carbide event. The γ' solvus for Mod-1 is comparable to that of CM247LC, though the dissolution window is larger. In addition, there remains an endothermic event near 600 °C, which is again attributed to γ' precipitation during first heating as the alloy seeks to approach the equilibrium phase fraction.

The microstructure of the Mod-1 alloy in the as-deposited (condition A) and aged (condition E) states was evaluated using SEM. Representative SEM micrographs are presented in Figure 12. The results show a significant increase in the propensity to cracking compared with CM247LC, with an average sample density of 99.04 ± 0.05 pct. In the A condition, the Mod-1 sample exhibited cracks that are similar in morphology to the cracks present in as-deposited CM247LC. A comparison of the crack morphologies has been provided in the Supplementary information, see Table S1. Previous studies support the observation that both solidification and liquation cracks are present in the microstructure.[14,19,20,22] The specimen in condition E shows evidence of recrystallisation, with grains showing uniform scattering contrast. The average sample density remained low in comparison to CM247LC, at 99.26 ± 0.05 pct. In comparison to the A condition, the cracks have increased in length but the average density has increased slightly.

The microstructure and phases present in the Mod-1 specimen were investigated further using TEM and STEM-EDX. The TEM analyses for specimens in conditions A and E are given in Figures 13 and 14 respectively. For the specimen in condition A, a high-angle grain boundary containing a crack was chosen for analysis. As Hf was removed and C significantly reduced in the Mod-1 composition, there was minimal EDX signal from these elements and they were therefore not included in the analysis. For the Mod-1 samples, there is significant segregation of Nb and Ti into bands. It is also observed that Co and W segregate away from these bands. Selected-area diffraction patterns taken from the matrix, shown in Figure 13, reveal the presence of weak γ' reflections. The TEM analysis for the Mod-1 specimen in the aged state (condition E) is shown in Figure 14 and reveals the presence of cuboidal γ' precipitates. In this sample, $M_{23}C_6$ carbides primarily rich in Cr, and to a lesser extent W, can be seen along the grain boundary. This phase was identified using selected-area diffraction patterns, one of which is shown in the figure.

Table III. The Elastic Constants, Poisson's Ratio (v), Effective Young's Modulus (E) and Effective Shear Modulus (G) for the L-PBF CM247LC Samples in Their Respective Post-Processed Conditions

Sample	(GPa)	(GPa)	(pct)	c_{11}	c_{22}	c_{33}	c_{12}	c_{13}	c_{23}	v	E c_{44}	G c_{55}	RMS c_{66}
CM247LC A	282	260	261	124	150	141	113	103	77	0.32	213	82	0.26
CM247LC E	306	258	306	125	180	148	100	103	79	0.33	217	83	0.72
CM247LC F	396	378	382	238	229	231	94	96	81	0.36	230	84	0.73

The elastic constants were calculated with sample dimensions for the RD, TD and BD representing the *x* (1), *y* (2) and *z* (3) axes, respectively. An RMS error describing the fit for elastic constants has been provided. An error of approximately ± 1 pct is associated with the C_{11} to C_{33} and C_{12} to C_{23} constants and an error of approximately ± 0.1 pct is associated with the C_{44} to C_{66} constants.
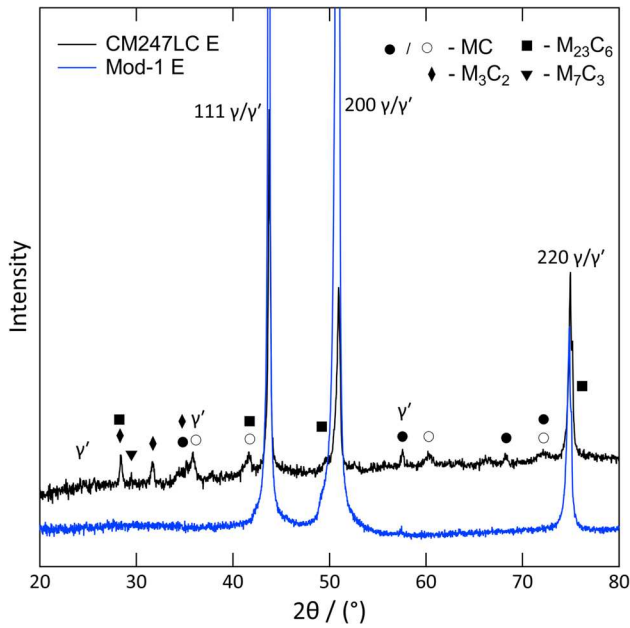

Fig. 10—XRD patterns of L-PBF CM247LC and Mod-1 in E condition, specified in Table II. The patterns have been vertically offset for clarity and the measured intensity is shown as √I. The peak positions of the primary phases present have been labelled. There are two distinct types of MC carbide present, with the filled circles corresponding to the (Ta/Ti)C reflections and the unfilled circles corresponding to the (HfTa)C. The positions for the γ matrix and γ′ superlattice peaks have been given with the primary reflections being labelled.

IV. DISCUSSION

The processing conditions of L-PBF often result in difficulties when processing Ni-based superalloys.[6,45] Such conditions often induce high thermal stresses in the material, which give rise to a variety of cracking processes.[16,24] This study, among others,[14,15,19] has shown that the fabrication of superalloy CM247LC using L-PBF results in cracking during deposition, typical of high γ′-containing alloys.[49,50] However, the main emphasis of this work was the subsequent evolution of the microstructure and the elastic properties of
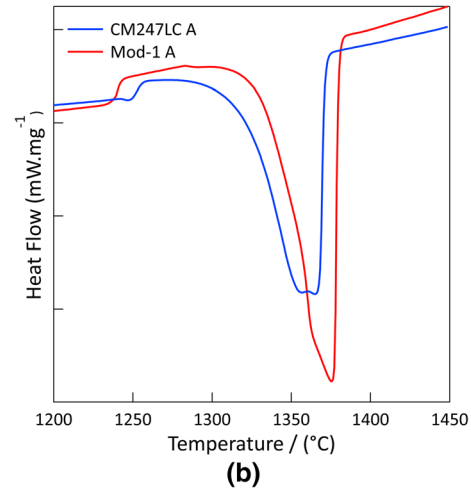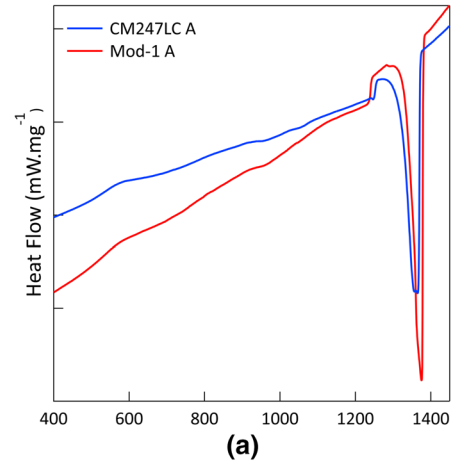

Fig. 11—(a) DSC traces for the first heating of L-PBF CM247LC and Mod-1 specimens in condition E from RT to 1450 °C. Each specimen has been labelled and offset for clarity. (b) A magnified section of the terminal region of the traces to highlight the differences between the samples on melting.

L-PBF CM247LC during each step of a standard post-processing routine.

Initial cracking in the L-PBF CM247LC specimen was believed to be solidification and liquation cracking based on the morphology of the cracks, see
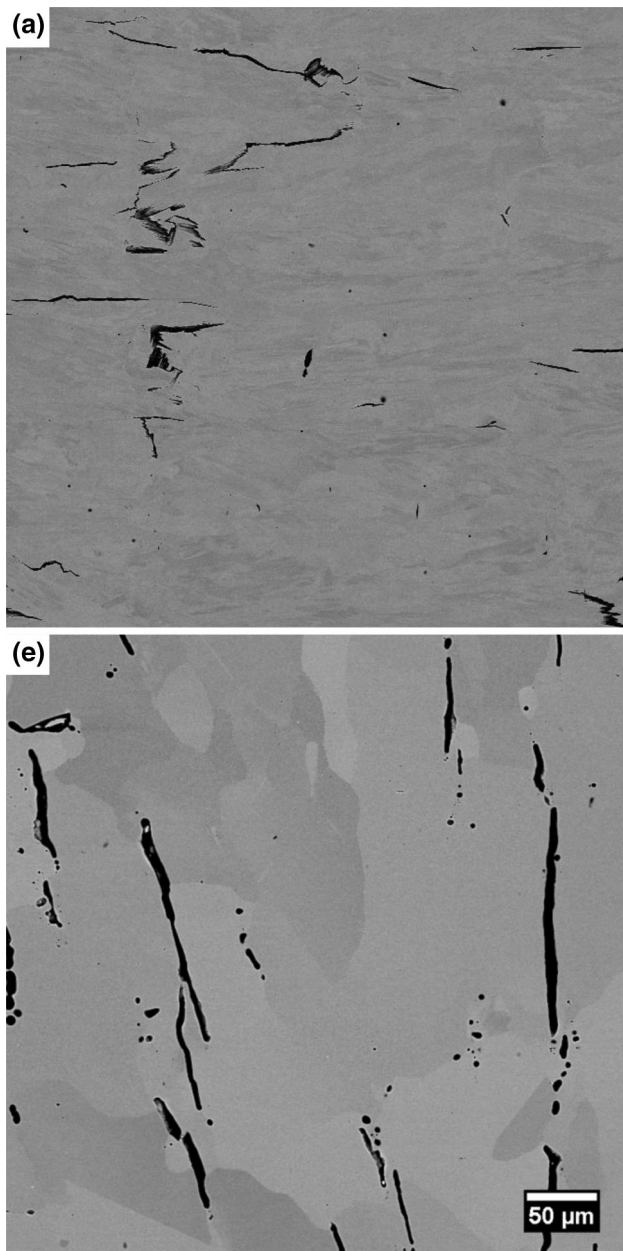
Fig. 12—SEM micrographs of L-PBF Mod-1 specimen in the A and E conditions.

Supplementary Figure S1 and Table S1. These types of cracking are typically associated with alloys having a large freezing range and a propensity to form low melting point phases.[16,24,25] It is well-known that the presence of B, C, Hf and Zr can increase the susceptibility to liquation cracking due the formation of low melting point phases.[18,19,26,49] However, the elements B, C and Hf can act as grain boundary strengtheners and may provide resistance to hot cracking.[19,45] Therefore, it is important to control the concentration of minority elements to avoid the formation of undesired phases whilst maintaining the grain boundary strength. For example, It has been shown by both Griffiths et al.[19] and Tang et al.[14] that removal of Hf whilst maintaining a reasonable carbon content can mitigate

microcracking in AM Ni-based superalloys. Similarly, a systematic study by Després et al.[37] highlighted that removal of Zr and control over the B and C content was essential in providing solidification cracking resistance. The authors stressed the importance of both the type and morphology of borides and carbides in addition to their location.

However, what is of greater importance is the level of thermal stresses experienced and the specific solidification behaviour of the alloy.[22,51] It has been described by both Zhang[47] and Kou et al.[22] that the stresses generated in the final stages of solidification are critical in determining susceptibility to hot cracking. Specifically, alloys that display sharp changes in the final fraction of liquid present are generally considered to be more susceptible to cracking. Following this concept, Tang et al.[14] successfully utilised the solidification cracking index presented by Kou et al.[22] to design alloys resistant to solidification cracking. An alternative approach has been adopted by other authors to reduce the susceptibility to this form of cracking by increasing the thermal resistance of the alloy through compositional modification.[21,52]

Whilst cracking was present in the as-deposited and as-blasted conditions (A and B), a significantly improved sample density was identified following HIP, suggesting that the HIP process was effective in reducing the fraction of solidification and liquation cracks, albeit isolated cases of solid-state cracking were observed. Notably, the modified CM247LC composition, Mod-1, was found to result in an increased cracking propensity. Whilst, the cracking mechanisms were not explored in detail, it is believed that the increased cracking propensity of Mod-1 is associated with the reduce fraction of the MC carbide phase as an overall reduction in elemental segregation and smaller freezing range was observed compared to CM247LC.

Of greater interest to this study were the several notable changes in the microstructure and phases present following each step of the post-processing treatments. The SEM analysis (Figure 2), XRD results (Figure 3) and TEM analysis (Figures 5 through 7) present a clear evolution in the morphology and type of carbides present in the microstructure. The initial occurrence of the MC-type carbides is expected and desired within the microstructure of this Ni-based superalloy.[50] However, the occurrence of the $M_{23}C_6$, as seen following processing step C, can present issues as these types of carbides deplete the microstructure of strengthening elements and serve as crack initiation points.[16,34,50] The presence of these carbides along the grain boundaries and intercellular regions might also explain the recrystallisation behaviour of the L-PBF CM247LC, Figure 8. Only partial recrystallisation was observed following solutioning at 1250 °C, condition D. Full recrystallisation only occurred when the specimens were exposed to a higher temperature of 1260 °C, condition F. This behaviour may be attributed to reduction in Zener drag pressure as a result of the further dissolution of γ' at the higher solution temperature.
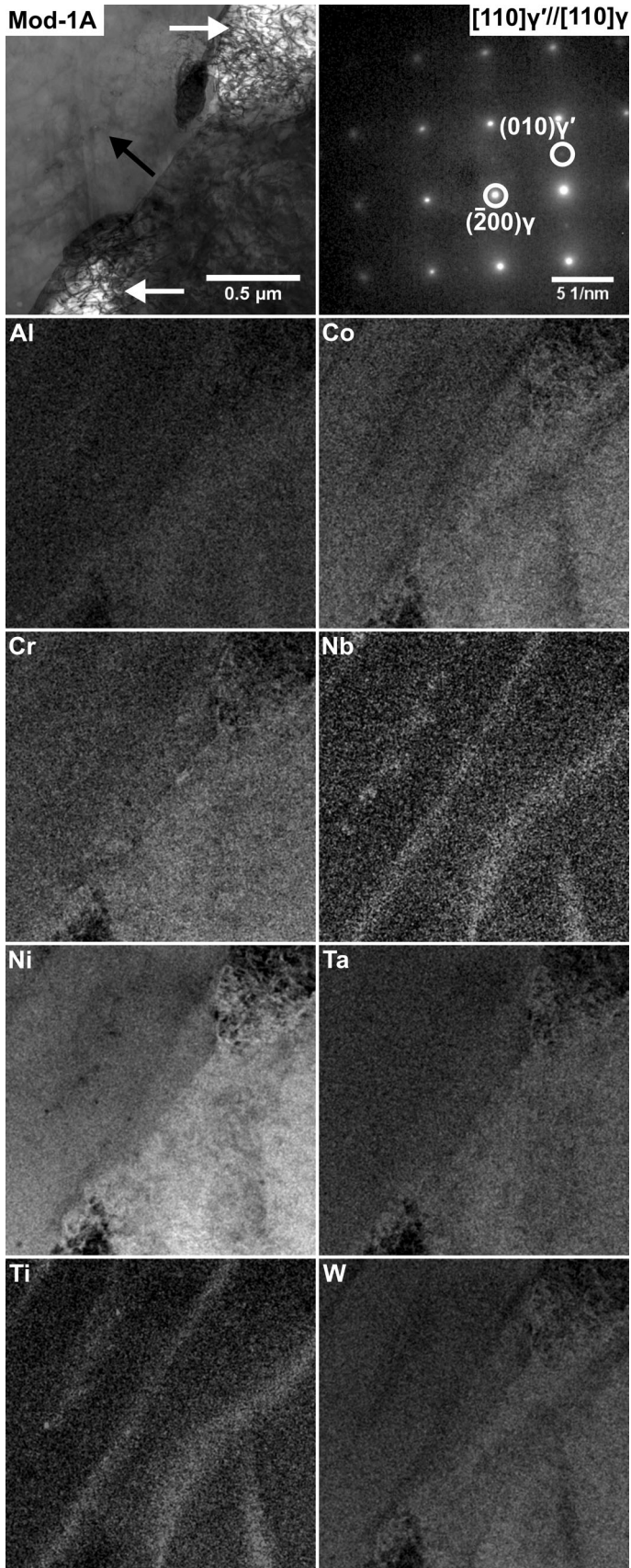
Fig. 13—TEM analysis of L-PBF Mod-1 in condition A. A bright field electron image is shown at the top left; accompanied by a selected-area electron diffraction pattern from the matrix along [100] at the top right with specific reflections identified. A black arrow has been added to the bright field image indicating the region where the SADP was taken from. Below are elemental distribution maps determined by STEM-EDX for the same field of view. Additional white arrows have been added to highlight the locations of the cracked regions.

The segregation of the strengthening elements in the as-deposited condition is of particular interest. The TEM analysis for the as-deposited specimen (Figure 5) indicates a clear difference in the degree of segregation along the high-angle grain boundary in comparison to the sub-grain/cellular regions. Notably, there is significant segregation of Hf and a depletion of Cr along the high-angle grain boundary. This could indicate the formation of a γ' film or continuous segregation zone forming at the terminal stages of solidification. It has been discussed in the literature that the formation of such a region could increase the susceptibility to solidification cracking.[14,19] Following condition E the segregation of Hf was eliminated (Figure 6), suggesting that this element had been effectively solutioned by the processing step. There were two visible morphologies of the γ', cuboidal and fan-type, the former occurring by conventional precipitation and the latter by discontinuous reaction. The fan-shaped γ' are irregular and will likely not yield the best performance in-service. As such, it is critical to ensure correct post-processing has been applied to the additively manufactured component to avoid their occurrence as more regular distribution and morphology of γ' precipitates are desirable for optimal properties.

The RUS results (Figure 9) show that isotropic elasticity was not achieved in the samples following the full recrystallisation. It is hypothesised that the remaining carbides influence the recrystallisation texture, consistent with previous reports.[12] Both the SEM-EBSD and RUS results present an interesting evolution of the texture during post-processing. The as-deposited condition is highly anisotropic (Table III). Following the full age of the L-PBF specimen, the anisotropy reduced with an axisymmetric symmetry in the elastic constants. However, residual anisotropy was retained that may be attributed to preferential grain growth along specific directions because of the inter-granular carbides that are expected to persist to the solution/recrystallisation temperatures. In certain applications where AM components are used, such anisotropic elastic properties may cause issues in-service. As a result, the elastic properties must be well understood if component integrity is to be assured.[12,45]

Comparing the results obtained from Mod-1 and CM247LC raises important considerations for future alloy design. Firstly, analysis of the XRD (Figure 10) and DSC (Figure 11) data for Mod-1 indicate that a reduction in the fraction of carbides formed within the

microstructure has been achieved along with a narrowing of the freezing range. Interestingly, the Hf-free variant of CM247LC proposed by Griffiths et al.[19] showed a greater narrowing of the freezing range when compared to standard CM247LC. The smaller reduction seen in this study is due to the addition of Nb and the lowering of C. The Nb was added to counteract the loss of Hf, preserving the fraction of γ' precipitates. It has been noted in welding research that having the correct C content is essential to preventing the formation of a low melting point eutectic. Whilst the reduction in the carbide fraction observed in Mod-1 may be linked to its increased cracking propensity, an improved recrystallisation performance was detected. Thus, this study, whilst inconclusive, has highlighted the importance of the carbide distributions in both cracking mechanisms and recrystallisation. Further work on the optimisation of carbide distributions is therefore essential to enable the effective tailoring of high γ' Ni-based superalloys to laser powder bed fusion.
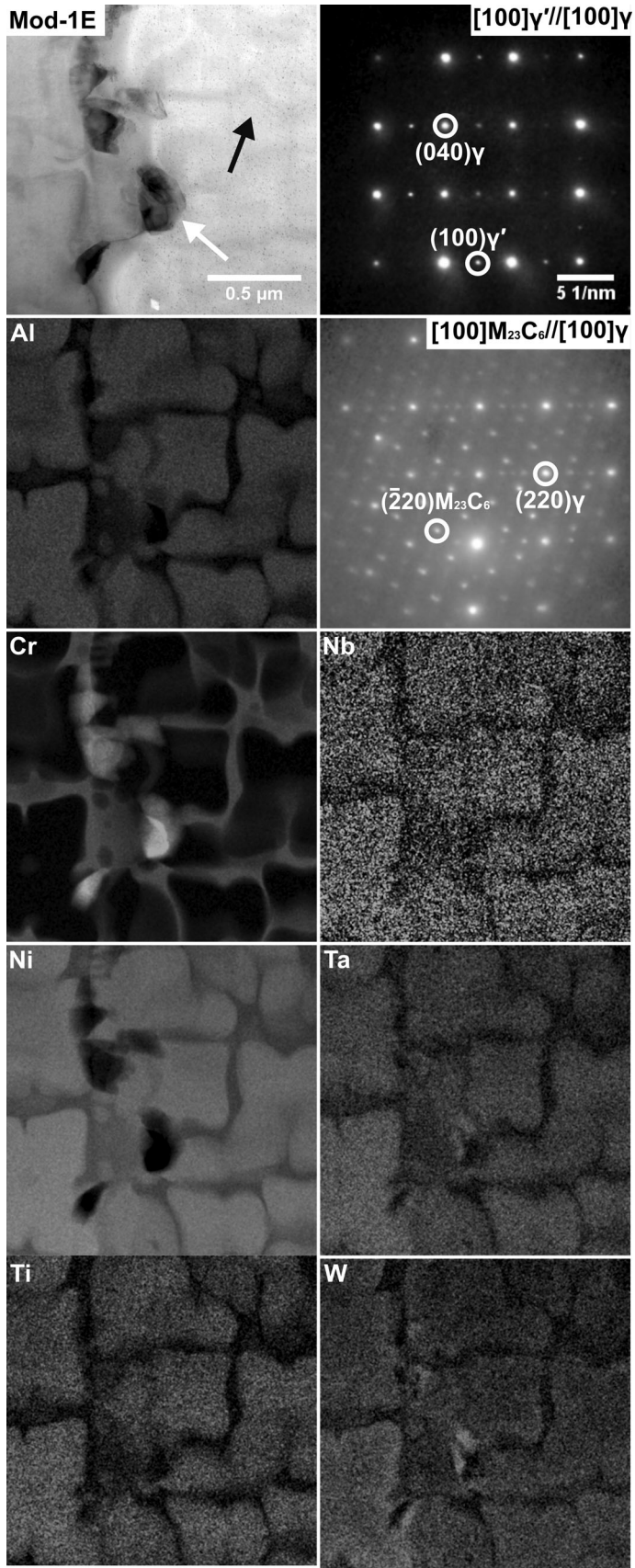
V. CONCLUSIONS

This study aimed to elucidate the microstructural evolution of CM247LC manufactured through L-PBF following each post-processing step. In the as-built condition, the occurrence of significant cracking was observed, consistent with solidification and liquation cracking. The presence of a Hf-rich, Cr-depleted region along the grain boundaries was identified through STEM-EDX and is likely a contributing factor to the extensive cracking observed in the material. Following the HIP and subsequent heat treatment steps there is evidence of crack closure.

The microstructural evolution of CM247LC during the standard post-processing steps used in this study demonstrate that the current post-processing regimen is not optimized for L-PBF CM247LC. Material in the final aged condition (E) has a partially recrystallized microstructure with a non-homogenous morphology and distribution of γ' precipitates. This further results in significant residual texture giving rise to anisotropic elastic properties.

The modification of the CM247LC composition through removal of Hf, reduction of C and addition of Nb did not reduce propensity to cracking during processing, even though the overall elemental segregation was indeed found to be significantly reduced. Mod-1 was instead observed to have a higher area fraction of cracking in all conditions compared to CM247LC. This increase is likely due to the modification of the carbides formed. Nevertheless, this allowed for recrystallisation at a lower temperature than in standard CM247LC. These results have highlighted the importance of the optimization of the carbide distributions as paramount in tailoring high γ' Ni-based superalloys for laser powder bed fusion.

Mod-1E

$[100]\gamma'//[100]\gamma$

$(040)\gamma$

$(100)\gamma'$

0.5 μm

5 1/nm

Al

$[100]M_{23}C_6//[100]\gamma$

$(\bar{2}20)M_{23}C_6$ $(220)\gamma$

Cr

Nb

Ni

Ta

Ti

W

◀ Fig. 14—TEM analysis of L-PBF Mod-1 in condition E. A bright field electron image is shown at the top left; accompanied by selected-area electron diffraction patterns for the matrix viewed along [100] at the top right and the $M_{23}C_6$ carbide, beneath, with specific reflections identified. Arrows have been added to the bright field image indicating where the SADPs originate, with the black arrow corresponding to the matrix and the white arrow corresponding to the carbides along the grain boundary. Below are elemental distribution maps determined by STEM-EDX for the same field of view.

CONFLICT OF INTEREST

The authors declare that they have no conflict of interest.

OPEN ACCESS

SUPPLEMENTARY INFORMATION

The online version contains supplementary material available at https://doi.org/10.1007/s11661-022-06939-0.

REFERENCES

1. S. Singamneni, Y. Lv, A. Hewitt, R. Chalk, W. Thomas, and D. Jordison: *J. Aeronaut. Aerosp. Eng.*, 2019, vol. 8, pp. 351–71.
2. Y. Zhang, L. Wu, X. Guo, S. Kane, Y. Deng, Y.-G. Jung, J.-H. Lee, and J. Zhang: *J. Mater. Eng. Perform.*, 2018, vol. 27, pp. 1–13.
3. S.S. Babu, N. Raghavan, J. Raplee, S.J. Foster, C. Frederick, M. Haines, R. Dinwiddie, M.K. Kirka, A. Plotkowski, Y. Lee, and R.R. Dehoff: *Metall. Mater. Trans. A*, 2018, vol. 49A, pp. 3764–80.
4. S.M. Thompson, L. Bian, N. Shamsaei, and A. Yadollahi: *Addit. Manuf.*, 2015, vol. 8, pp. 36–62.
5. A. Basak: *Paper Presented at 30th Annual International Solid Freeform Fabrication Symposium - An Additive Manufacturing Conference, SFF 2019*, Austin, United States, 2019.
6. M.M. Attallah, R. Jennings, X. Wang, and L.N. Carter: *MRS Bull.*, 2016, vol. 41, pp. 758–64.
7. W.J. Sames, F. Medina, W.H. Peter, S.S. Babu, and R.R. Dehoff: Pittsburgh, PA, 2014, vol. 409–23.
8. M. Haines, A. Plotkowski, C.L. Frederick, E.J. Schwalbach, and S.S. Babu: *Comput. Mater. Sci.*, 2018, vol. 155, pp. 340–49.
9. N. Nadammal, S. Cabeza, T. Mishurova, T. Thiede, A. Kromm, C. Seyfert, L. Farahbod, C. Haberland, J.A. Schneider, P.D. Portella, and G. Bruno: *Mater. Des.*, 2017, vol. 134, pp. 139–50.
10. A. Ramakrishnan and G.P. Dinda: *Mater. Sci. Eng. A*, 2019, vol. 740–741, pp. 1–13.
11. H. Wang, X. Zhang, G.B. Wang, J. Shen, G.Q. Zhang, Y.P. Li, and M. Yan: *J. Alloy Compd.*, 2019, vol. 807, p. 151662.
12. J.F.S. Markanday, M.A. Carpenter, N.G. Jones, R.P. Thompson, S.E. Rhodes, C.P. Heason, and H.J. Stone: *Mater. Sci. Eng. A*, 2021, vol. 825, p. 141781.
13. J.F.S. Markanday, M.A. Carpenter, N.G. Jones, R.P. Thompson, S.E. Rhodes, C.P. Heason, and H.J. Stone: *Data Brief*, 2021, vol. 39, p. 107570.
14. Y.T. Tang, C. Panwisawas, J.N. Ghoussoub, Y. Gong, J.W.G. Clark, A.A.N. Németh, D.G. McCartney, and R.C. Reed: *Acta Mater.*, 2021, vol. 202, pp. 417–36.
15. J.H. Boswell, D. Clark, W. Li, and M.M. Attallah: *Mater. Des.*, 2019, vol. 174, p. 107793.
16. J.N. DuPont, J.C. Lippold, and S.D. Kiser: *Welding Metallurgy and Weldability of Nickel-Base Alloys*, vol. 14, Wiley, Hoboken, 2009, p. 440.
17. X. Zhang, H. Chen, L. Xu, J. Xu, X. Ren, and X. Chen: *Mater. Des.*, 2019, vol. 183, p. 108105.
18. Y.S. Lee, M.M. Kirka, J. Ferguson, and V.C. Paquit: *Addit. Manuf.*, 2020, vol. 32, p. 101031.
19. S. Griffiths, H. Ghasemi Tabasi, T. Ivas, X. Maeder, A. De Luca, K. Zweiacker, R. Wróbel, J. Jhabvala, R.E. Logé, and C. Leinenbach: *Addit. Manuf.*, 2020, vol. 36, p. 101443.
20. J. Xu, X. Lin, Y. Zhao, P. Guo, X. Wen, Q. Li, H. Yang, H. Dong, L. Xue, and W. Huang: *Metall. Mater. Trans. A*, 2018, vol. 49A, pp. 5118–36.
21. N.J. Harrison, I. Todd, and K. Mumtaz: *Acta Mater.*, 2015, vol. 94, pp. 59–68.
22. S. Kou: *Acta Mater.*, 2015, vol. 88, pp. 366–74.
23. B. Ruttert, M. Ramsperger, L. Mujica Roncery, I. Lopez-Galilea, C. Körner, and W. Theisen: *Mater. Des.*, 2016, vol. 110, pp. 720–27.
24. T. Boellinghaus and H. Herold: *Hot Cracking Phenomena in Welds*, Springer, Berlin, 2005.
25. T. Boellinghaus, H. Herold, C.E. Cross, and J.C. Lippold: *Hot Cracking Phenomena in Welds II*, Springer, Berlin, 2008, p. 467.
26. S. Griffiths, H. Ghasemi-Tabasi, A. De Luca, J. Pado, S.S. Joglekar, J. Jhabvala, R.E. Logé, and C. Leinenbach: *Mater. Charact.*, 2021, vol. 171, p. 110815.
27. A. Migliori and J. Sarrao: *Resonant Ultrasound Spectroscopy: Applications to Physics, Material Measurements and Nondestructive Evaluation*, Wiley, New York, 1997.
28. R.E.A. McKnight, T. Moxon, A. Buckley, P.A. Taylor, T.W. Darling, and M.A. Carpenter: *J. Phys.*, 2008, vol. 20, p. 075229.
29. A. Marmier, Z.A.D. Lethbridge, R.I. Walton, C.W. Smith, S.C. Parker, and K.S. Evans: *Comput. Phys. Commun.*, 2010, vol. 181, pp. 2102–15.
30. P. Ravindran, L. Fast, P.A. Korzhavyi, B. Johansson, J. Wills, and O. Eriksson: *J. Appl. Phys.*, 1998, vol. 84, pp. 4891–4904.
31. C. Qiu, H. Chen, Q. Liu, S. Yue, and H. Wang: *Mater. Charact.*, 2019, vol. 148, pp. 330–44.
32. J.C. Lippold, T. Boellinghaus, and C.E. Cross: *Hot Cracking Phenomena in Welds III*, Springer, Berlin, 2011.
33. M. Zhong, H. Sun, W. Liu, X. Zhu, and J. He: *Scripta Mater.*, 2005, vol. 53, pp. 159–64.

34. R. Muñoz-Moreno, V.D. Divya, S.L. Driver, O.M.D.M. Messé, T. Illston, S. Baker, M.A. Carpenter, and H.J. Stone: *Mater. Sci. Eng. A*, 2016, vol. 674, pp. 529–39.
35. V.D. Divya, R. Muñoz-Moreno, O.M.D.M. Messé, J.S. Barnard, S. Baker, T. Illston, and H.J. Stone: *Mater. Charact.*, 2016, vol. 114, pp. 62–74.
36. W. Chen, M.C. Chaturvedi, and N.L. Richards: *Metall. Mater. Trans. A*, 2001, vol. 32A, pp. 931–39.
37. A. Després, S. Antonov, C. Mayer, C. Tassin, M. Veron, J.-J. Blandin, P. Kontis, and G. Martin: *Materialia*, 2021, vol. 19, p. 101193.
38. X. Wang, L.N. Carter, B. Pang, M.M. Attallah, and M.H. Loretto: *Acta Mater.*, 2017, vol. 128, pp. 87–95.
39. X. Wei, M. Xu, Q. Wang, M. Zhang, W. Liu, J. Xu, J. Chen, H. Lu, and C. Yu: *Mater. Des.*, 2016, vol. 110, pp. 90–98.
40. B. Sreenu, R. Sarkar, S.S.S. Kumar, S. Chatterjee, and G.A. Rao: *Mater. Sci. Eng. A*, 2020, vol. 797, p. 140254.
41. Q. Tan, G. Zhu, W. Zhou, Y. Tian, L. Zhang, A. Dong, D. Shu, and B. Sun: *J. Alloy Compd.*, 2022, vol. 913, p. 165196.
42. D. Ma, A.D. Stoica, Z. Wang, and A.M. Beese: *Mater. Sci. Eng. A*, 2017, vol. 684, pp. 47–53.
43. Y.H. He, X.Q. Hou, C.H. Tao, and F.K. Han: *Eng. Fail. Anal.*, 2011, vol. 18, pp. 944–49.
44. L. Zhuo, M. Liu, Q. Chen, S. Liang, J. Xiong, and F. Wang: *Mater. Sci. Technol.*, 2018, vol. 34, pp. 334–39.
45. J.F.S. Markanday: *Mater. Sci. Technol.*, 2022, pp. 1–15.
46. R. Engeli, T. Etter, and F. Geiger: United States of America, 2017, 20170356068.
47. J. Zhang: *Scripta Mater.*, 2003, vol. 48, pp. 677–81.
48. J.O. Andersson, T. Helander, L. Höglund, P. Shi, and B. Sundman: *Calphad*, 2002, vol. 26, pp. 273–331.
49. J.C. Lippold: *Welding Metallurgy and Weldability*, vol. 17, Wiley, Hoboken, 2015, p. 400.
50. R.C. Reed: *The Superalloys: Fundamentals and Applications*, vol. 14, Cambridge University Press, Cambridge, 2006, p. 372.
51. C. Li, Z.Y. Liu, X.Y. Fang, and Y.B. Guo: *Procedia CIRP*, 2018, vol. 71, pp. 348–53.
52. B.D. Conduit, T. Illston, S. Baker, D.V. Duggappa, S. Harding, H.J. Stone, and G.J. Conduit: *Mater. Des.*, 2019, vol. 168, p. 107644.